Comparative Analysis of 5-band and 10-band Multispectral Drone Imagery for Salt Marsh Vegetation Mapping

Gregory S. Norris[1], Brigitte Leblon[2], Armand LaRocque[1], Myriam A. Barbeau[3], Alan R. Hanson[4]

[1] Faculty of Forestry and Environmental Management, University of New Brunswick, Fredericton, NB, Canada, E3B 5A3 - (gnorris1, larocque)@unb.ca

[2] Faculty of Natural Resource Management, Lakehead University, Thunder Bay, ON P7B 5E1, Canada - bleblon@lakeheadu.ca

[3] Department of Biology, University of New Brunswick, Fredericton, NB, Canada, E3B 5A3 - mbarbeau@unb.ca

[4] Canadian Wildlife Service, Environment Canada, P.O. Box 6227, Sackville, NB, Canada, E4L 4N1 - al.hanson@canada.ca

Keywords: Multispectral Imaging Sensors; Uncrewed Aerial Vehicle (UAV); Random Forest; Salt marsh.

Abstract

Multispectral drone sensors enable fine-scale ecological mapping, but added bands can inflate processing costs. We evaluated the MicaSense RedEdge-MX Red and Blue cameras (5 bands each) versus the Dual Camera System (10 bands) for vegetation mapping in two salt marsh sites in Aulac, New Brunswick, Canada (24 classes at the reference site; 15 at the restoration site). Pixel-based Random Forest (RF) classifications were used to compare validation accuracy, variable importance, and processing time for stitching and classification. Five-band maps achieved up to 95% validation accuracy; the 10-band configuration improved accuracy by ≤2%. Band contributions were site dependent: the near-infrared (NIR) band from the Red camera aided classification at the reference site, whereas additional red-edge bands in the Blue/Dual setups improved performance at the restoration site. However, stitching time rose sharply for the Blue and Dual systems, and RF classification time scaled with data volume and class complexity. Overall, the 5-band Red camera provided a cost-effective balance of accuracy and efficiency, offering practical guidance for sensor selection in drone-based salt marsh monitoring.

1 Introduction

The development of remote sensing technologies has greatly expanded our ability to monitor and analyse environmental and ecological patterns. The progression from aircraft- to satellite-based systems, and more recently to uncrewed aerial vehicles (UAVs or drones), has transformed data acquisition in remote sensing (Cracknell, 2018). Satellites offer broad spatial and temporal coverage suited to large-scale, long-term monitoring (Liao et al., 2020), whereas drones provide very high spatial resolution for site-specific studies (Cracknell, 2018; Zheng et al., 2022). This advancement has coincided with a shift from simple Red-Green-Blue (RGB) cameras to multispectral and hyperspectral sensors, which capture a wider range of wavelengths and allow more precise land-cover characterization (Xing et al., 2019).

Traditional RGB sensors are limited in distinguishing vegetation types because they record only visible light. Multispectral sensors, by contrast, capture data across specific wavelengths—including near-infrared and red-edge—providing stronger spectral discrimination for vegetation and land-cover mapping (Ahmed et al., 2017). Drone-mounted multispectral sensors are especially valuable for salt marsh studies, enabling fine-scale monitoring of vegetation composition and condition (Huang et al., 2023; Nardin et al., 2021; Doughty & Cavanaugh, 2019). Near-infrared and red-edge wavelengths are particularly useful for identifying vegetation types (Zhang et al., 2021), assessing water and soil properties (McEliece et al., 2020; Anne et al., 2014), and calculating vegetation indices that track plant health and productivity (Nardin et al., 2021). The selection of wavebands is therefore a critical consideration in salt marsh monitoring (Gitelson et al., 2003; Mutanga & Skidmore, 2004).

Integrating data from multiple multispectral bands and platforms enhances environmental monitoring, especially in dynamic systems like salt marshes (Zhang et al., 2021; LaRocque et al., 2020; Slagter et al., 2020). However, increasing the number of bands and spatial resolution also raises data volume and computational complexity, which can reduce model efficiency (Gilbertson & Van Niekerk, 2017). In this study, merging imagery from two 5-band cameras into a 10-band dataset required additional processing time and computational power to manage larger file sizes. To address these challenges, researchers often reduce dimensionality, select key features, or use classifiers that handle high-dimensional data effectively (Zheng et al., 2022; Sun et al., 2021). Balancing spectral detail and processing efficiency is therefore essential for producing accurate yet practical classifications within computational limits.

The present study examined how the number and wavelength range of multispectral bands influence classification accuracy and processing efficiency when mapping vegetation of Atlantic Canadian salt marshes. Specifically, we compared the performance of UAV images acquired with a 5-band MicaSense RedEdge-MX Red or Blue camera with the combined 10-band Dual Camera System. Building on Norris et al. (2024), who studied these same sites and showed that pixel-based classification outperformed object-based methods, we applied a Random Forest classifier using spectral and textural features to assess how band configuration affects mapping outcomes. Multitemporal imagery from June, July, and August 2021 was used to capture seasonal variation, which improves classification reliability in highly dynamic environments (Li et al., 2018; Klemas, 2013). By comparing classification accuracy and processing time across configurations, this study identifies trade-offs between sensor complexity and efficiency, offering practical guidance for selecting multispectral cameras in drone-based wetland monitoring.

This contribution has been peer-reviewed. The double-blind peer-review was conducted on the basis of the full paper.
https://doi.org/10.5194/isprs-annals-XI-M-1-2026-39-2026

2 Materials and methods

2.1 Study area

The study area is in Aulac, New Brunswick, Canada, at the head of the Cumberland Basin in the Bay of Fundy (45°51′31″N, 64°18′16″W; Figure 1). The region experiences semi-diurnal tides of 7–13 m (Desplanque & Mossman, 2004) and contains a managed-realignment restoration project initiated in 2009–2010 (see Norris et al., 2024 and references therein). Two sites were examined: a reference marsh (Site A) and a restoration marsh (Site B). The restoration site is dominated by *Spartina alterniflora*, whereas the reference site is dominated by *S. patens*, with additional species such as *Puccinellia maritima*, *Triglochin maritima*, and *Spartina pectinata* contributing to vegetation diversity represented in the sites.

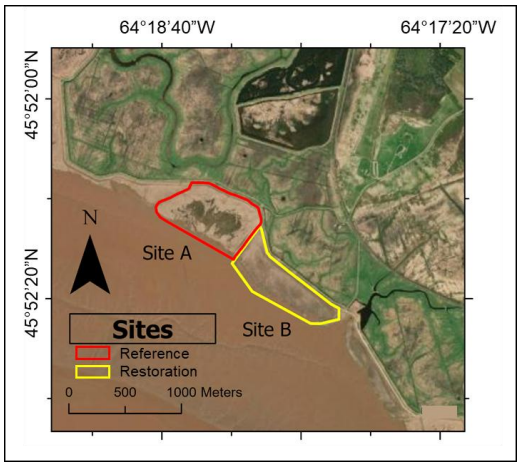

Figure 1. Location of studied salt marshes in Aulac, New Brunswick, on a Google Earth™ image; details include restoration sites (outlined in yellow) and reference sites (red).

2.2 Field data and land-cover classes

Field data used for training and validation followed the protocol in Norris et al. (2024). Stratified random sampling was conducted along 3–4 transects per site using 15 quadrats (0.5 × 0.5 m) per transect during June, July, and August 2021. GPS coordinates, vegetation type, stem counts, and ground photographs were recorded at each quadrat, with additional samples collected along site perimeters to capture full class variability. Across both sites, 30 land-cover classes were identified, including six single-species monocultures, three mixed vegetation assemblages, six abiotic features (e.g., bare mud, rocks, driftwood), five water-associated classes, and ten classes showing seasonal change (Norris et al., 2024). Fifteen classes occurred at the restoration site, 24 at the reference site, and nine were shared. Mixed assemblages were retained in the training data to reflect the natural heterogeneity of salt marsh vegetation.

2.3 Image acquisition

Multispectral imagery was acquired using a DJI Matrice 200 V2 equipped with a MicaSense Dual Camera System comprising the RedEdge-MX Red and RedEdge-MX Blue cameras (Norris et al., 2024). Each camera captured five bands at 1.2 MP resolution. The Red camera included red, green, blue, red-edge, and near-infrared (NIR) bands, whereas the Blue camera included blue, green, red, and two red-edge bands, omitting NIR (Table 1). Bands from each camera were processed separately to create 5-band Red and Blue datasets and combined to form the 10-band set for comparison.

Table 1. Spectral characteristics of the five bands acquired by the RedEdge-MX Red and RedEdge-MX Blue cameras in the MicaSense Dual-Camera system.

Camera	Band name	Center of Wavelength (μm)	Band-width (μm)
RedEdge-MX Red	Blue 475	475	32
	Green 560	560	27
	Red 668	668	14
	Red-Edge 717	717	12
	NIR 842	842	57
RedEdge-MX Blue	Coastal Blue 444	444	28
	Green 531	531	14
	Red 650	650	16
	Red-Edge 705	705	10
	Red-Edge 740	740	18

Flights were conducted at 100 m altitude and 10 m s^{-1} speed, producing ≈7.3 cm spatial resolution. Imagery was collected near solar noon and low tide to minimize shadows and ensure full site exposure. Flight paths were oriented perpendicular to solar illumination, with consistent lighting conditions (<10% cloud in June; full overcast in July–August). Reflectance calibration used a MicaSense Spectralon panel (RP04-1949202-OB).

2.4 Pre-classification image processing

Imagery was processed in Pix4Dmapper to produce georeferenced reflectance mosaics, which were orthorectified using fixed landmarks and stacked across June–August 2021 for multitemporal analysis (Figure 2). From these mosaics, vegetation indices (VIs) and textural features were derived following Norris et al. (2024). Thirteen VIs were calculated for the 5-band Red imagery, none for the Blue (no NIR), and 28 for the 10-band dataset. Ten GLCM (Gray Level Co-occurrence Matrix) texture metrics were computed per band (Homogeneity, Contrast, Dissimilarity, Mean, SD, Entropy, Angular second moment, Correlation, GLDV ASM, GLDV Entropy; Haralick et al., 1973).

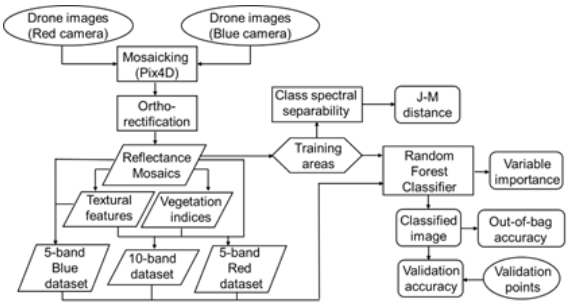

Figure 2. Flowchart of method used for processing multispectral drone images. Circles represent input data, square boxes processing steps, diamond-shaped boxes image products that are subsequently analyzed, and rounded boxes the final outcomes.

In total, the models used 204 input features for the Red camera (15 bands, 39 VIs, 150 textures), 165 for the Blue (15 bands, 150 textures), and 414 for the 10-band setup (30 bands, 84 VIs, 300 textures). Feature sets were tailored to each camera's spectral range to allow fair within-system comparison.

This contribution has been peer-reviewed. The double-blind peer-review was conducted on the basis of the full paper.
https://doi.org/10.5194/isprs-annals-XI-M-1-2026-39-2026 | © Author(s) 2026. CC BY 4.0 License.

2.5 Random Forest classification

Training and validation areas for each land-cover class were delineated following Norris et al., (2024). The number of polygons per class ranged from 5–60 depending on class extent. Training and validation points were distributed across both sites to capture class variability. Although validation points were often near training areas, they were selected independently to minimize spatial overlap. An even 50/50 split between training and validation samples was used for model development and accuracy assessment.

Spectral separability among classes was evaluated using Jeffries-Matusita (JM) distance on the 10-band imagery. Some low separability values were observed among spectrally similar vegetation types, emphasizing the value of incorporating multitemporal, textural, and index-based features to enhance class distinction.

All Random Forest (RF) classifications were performed in R (Norris et al., 2024) using 500 trees and the default *mtry* value (square root of the number of predictors). This configuration is widely used in remote sensing due to its stability and accuracy in high-dimensional datasets without extensive parameter tuning. RF's embedded feature selection and bootstrap aggregation reduce sensitivity to variable redundancy and overfitting, although computational time increases with larger feature sets.

2.6 Model testing and classification accuracy assessment

Classifier performance was evaluated using both internal and independent validation methods. Out-of-bag (OOB) accuracy from the Random Forest model provided an internal measure of classification reliability, while confusion matrices were used to calculate overall, user's, and producer's accuracies, as well as kappa coefficients.

Independent validation was conducted using field data collected at each site. Class values from the classified maps were extracted to the validation points using the Extract Values to Points tool in ArcMap®, allowing direct comparison between predicted and observed land-cover classes. This two-stage approach using OOB validation and field-based accuracy assessment provided a comprehensive evaluation of model performance.

2.7 Variable importance in the classification

RF was used to evaluate the relative importance of each image feature in the classification models. Variable importance was quantified using the mean decrease in accuracy, calculated by randomly permuting the values of each feature and measuring the resulting drop in OOB classification accuracy. Features causing larger decreases were considered more important. Variable importance outputs were ranked from highest to lowest and visualized using horizontal bar graphs showing the top 10 most influential features for each camera setup.

To facilitate interpretation, a structured naming convention was applied. Raw reflectance features were labeled as Band_Month (e.g., RedEdge740_August), vegetation indices as Index_Month (e.g., NDVI_July), and texture metrics as Band_Texture(Metric)_Month (e.g., RedEdge717_TextureMean_August). This format identifies each feature's spectral source, texture calculation, and month of image acquisition.

2.8 Analysis of processing times

Processing time and computational requirements were compared among the three camera setups (5-band Red, 5-band Blue, and 10-band Dual). Imagery from identical sites and months was processed in Pix4Dmapper for consistency. The Red and Blue cameras produced 3,500–4,300 images per site, while the Dual Camera System produced 7,400–8,800 images. Due to the large file size, Dual Camera mosaics were processed in two halves and merged, whereas single-camera datasets were completed in one run. Total processing time for the Dual Camera System included this additional merge step. All mosaicking was performed on a high-performance workstation (128 GB RAM, 256 GB virtual memory).

Classification processing times were also compared across camera setups. Random Forest models were executed on a secondary system (16 GB RAM, 3 GB virtual memory). The broader spectral range of the Dual Camera System allowed for additional vegetation indices but increased processing duration. These comparisons provided a standardized assessment of computational efficiency among setups.

3 Results

3.1 Image classification and internal model performance

OOB accuracies exceeded 99.5% across all camera setups, indicating very strong internal model performance. Classified outputs from the 5-band Red, 5-band Blue, and 10-band Dual configurations produced nearly identical spatial patterns, demonstrating model robustness despite large differences in input-feature volume (165–414 features). Because the 10-band results were visually representative of all configurations, only these maps are shown (Figure 3–4). The Dual system achieved slightly higher OOB accuracy for certain vegetation classes, but overall differences among setups were negligible. As OOB accuracy can overestimate model performance in highly complex classification problems (Breiman, 2001), independent validation was used to more reliably assess classification performance.

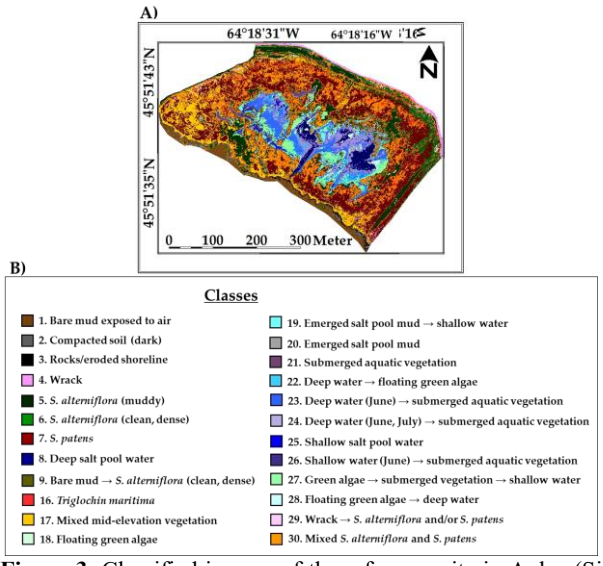

Figure 3. Classified images of the reference site in Aulac (Site A) created using a RF classifier applied to the (A) 10-band Dual camera dataset acquired on 13 June, 12 July, and 10 August 2021 to map 24 classes listed in (B).

This contribution has been peer-reviewed. The double-blind peer-review was conducted on the basis of the full paper.
https://doi.org/10.5194/isprs-annals-XI-M-1-2026-39-2026 | © Author(s) 2026. CC BY 4.0 License.

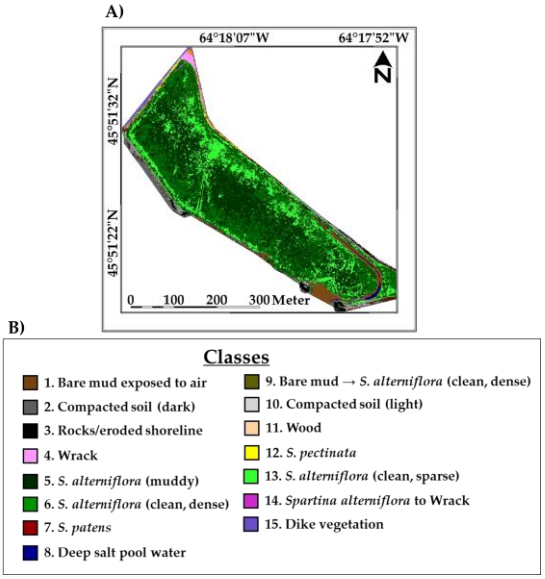

Figure 4. Classified images of the restoration site in Aulac (Site B) created using a RF classifier applied to the (A) 10-band Dual camera dataset acquired on 13 June, 12 July, and 10 August 2021 to map 15 classes listed in (B).

3.2 Validation data using independent field data

Independent validation using field data confirmed that differences in classification accuracy among the three camera setups were minimal, with overall accuracies varying by less than 2% (Table 2). For the reference site (Site A), both the 5-band Red and 10-band Dual classifications achieved comparable overall accuracy, while the 5-band Blue classification performed slightly lower. Most discrepancies were associated with *Spartina alterniflora* classes, which showed reduced user's and producer's accuracies in the Blue dataset. Classes that exhibited seasonal variation also produced more commission and omission errors in the Blue camera results. For the restoration site (Site B), the 5-band Red, 5-band Blue, and 10-band classifications achieved overall accuracies of 94.5%, 95.0%, and 95.2%, respectively, again showing only marginal improvement with additional bands. Overall, these results indicate that increasing spectral dimensionality from five to ten bands provided only minor gains in classification accuracy, suggesting that simpler 5-band systems may be sufficient for efficient salt marsh mapping.

Table 2. Comparison of field validation classification accuracies for 5-band Red, 5-band Blue, and 10-band Dual camera image datasets for the reference (Site A) and restoration (Site B) sites computed by a RF classifier. AA = Average Accuracy, OA = Overall Accuracy, KC = Kappa Coefficient.

Site	Site A			Site B		
Camera	AA	OA	KC	AA	OA	KC
Red	93.8	92.4	91.9	94.6	94.5	94.1
Blue	90.9	90.4	89.7	94.9	95.0	94.6
Dual	93.9	92.4	91.9	95.5	95.2	94.8

3.3 Variable importance in the classification

Across all classifications (Figures 5 & 6), textural features were consistently the most influential predictors, followed by raw reflectance bands, while vegetation indices contributed minimally. Among the highest-ranked variables for the 10-band classifications, a greater proportion originated from the Red camera, particularly at the reference site (Site A). In contrast, features from the Blue camera were more evenly represented at the restoration site (Site B).

When considering the 5-band classifications, the rankings largely mirrored those of the 10-band results. Vegetation indices (derived only from the Red camera) were rarely among the top-ranked variables, confirming their limited role in improving classification performance at either site. Textural features dominated the rankings in every case, especially those derived from tonal-mean calculations, underscoring the importance of spatial pattern information over additional spectral bands for distinguishing salt marsh vegetation types.

Across months, most influential features were derived from August imagery, reflecting peak seasonal contrast among vegetation classes. June imagery contributed less frequently, except in the 5-band Red classification of Site A.

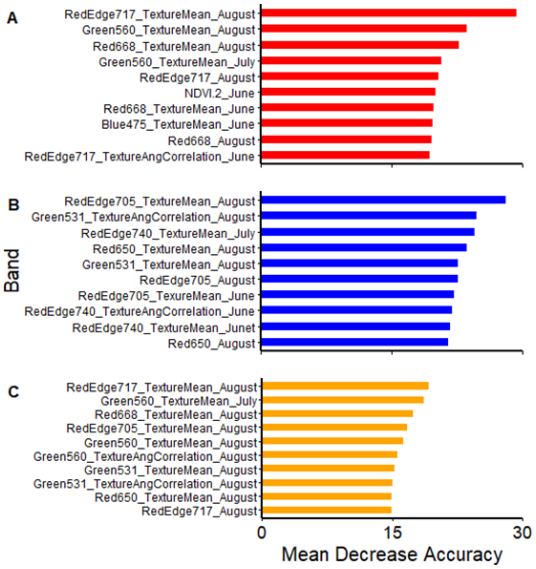

Figure 5. For the reference site (Site A), top 10 input features (Bands) ranked according to the mean decrease in OOB accuracy, to compare the (A) 5-band Red camera and (B) 5-band Blue camera multitemporal images to the (C) 10-band Dual camera set.

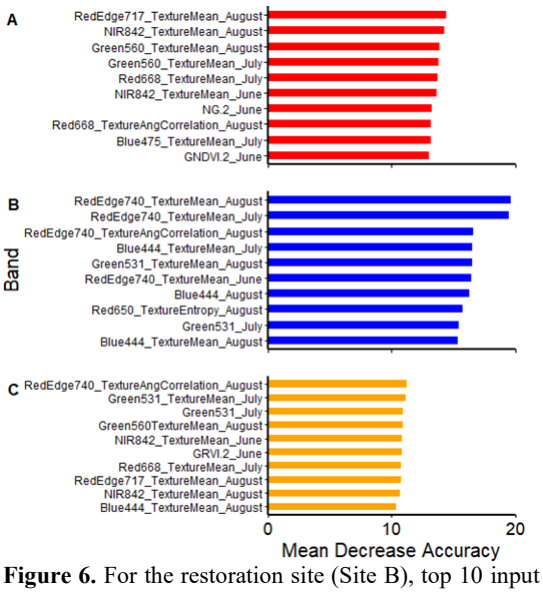

Figure 6. For the restoration site (Site B), top 10 input features (Bands) ranked according to mean decrease accuracy, to compare the (A) 5-band Red camera and (B) 5-band Blue

camera multitemporal images to the (C) 10-band Dual camera set.

3.4 Processing time for orthomosaic construction and image classification

Processing times differed substantially among camera setups (Figure 7). The 5-band Red camera produced the fastest orthomosaic results, requiring less than two hours per site, while the Blue camera averaged over 25 hours despite similar image counts (≈3,500–4,300). The 10-band Dual Camera System took the longest (over 32 hours) largely due to the need to process each site in halves and merge the outputs because of file-size limitations. For classification, Random Forest processing time increased with the number of input features: the 5-band Blue setup finished most quickly, followed by the Red, and the 10-band configuration required roughly 2–3× longer to classify the same area. Shorter times for the restoration site (Site B) reflected its smaller mosaic size and fewer land-cover classes. Overall, processing duration scaled directly with image volume, number of bands, and class complexity, indicating that optimizing band selection can substantially reduce computational costs without compromising classification accuracy.

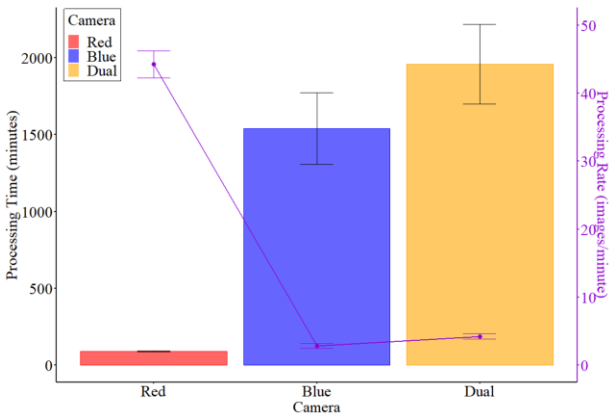

Figure 7. Mean (± SE) processing time and rate for orthomosaic construction (using Pix4D Mapper) for each camera system: the MicaSense 5-band RedEdge-MX Red camera (Red), the MicaSense 5-band RedEdge-MX Blue camera (Blue), and the MicaSense 10-band Dual Camera System (Dual). Bars are processing time; line is processing rate. Number of images processed was 3,500–4,300 for the Red and Blue cameras, and 7,400–8,800 for the Dual Camera System. n = 6 independent runs for each camera system; a "run" corresponds to the stitching of images for a given site (Sites A or B) and month combination in 2021.

4 Discussion

4.1 Costs and benefits of using a 5-band compared to a 10-band multispectral image set

The present study built on previous research applying multispectral drone imagery for mapping land-cover distributions in a restoring and reference salt marsh in Aulac, New Brunswick, Canada (Norris et al., 2024). We assessed how changes in spectral configuration (5-band RedEdge-MX Red, 5-band RedEdge-MX Blue, and 10-band Dual Camera System), vegetation indices, and textural features affected classification accuracy and processing efficiency. These sensors are established tools for wetland and vegetation mapping (Nardin et al., 2021; Doughty & Cavanaugh, 2019; Wang, 2021), and our comparison refines understanding of their relative strengths and trade-offs. Field validation showed only small accuracy differences: the 10-band system reached 92.4% and 95.2% for Sites A and B, while the 5-band Red achieved 92.4% and 94.5%, and the 5-band Blue 90.4% and 95.0%. Such minor variation indicates that simpler sensors can perform comparably to more complex systems.

The near-infrared (NIR) band, included only in the Red camera, aided classification of dominant vegetation at the reference site but contributed little on its own, as it was absent from the top 25 most important features—likely due to small leaf area and similar NIR reflectance among salt marsh species (Artigas & Yang, 2006). In contrast, red-edge bands consistently ranked highest and have proven valuable for intertidal environments (Turpie, 2013) and *Spartina* species discrimination (Artigas & Yang, 2006). Green and red bands were also influential, while blue bands appeared infrequently, probably due to reduced water presence during low-tide flights. The 5-band Blue camera performed unexpectedly well at the restoration site, suggesting its additional red-edge band improved separation between *Spartina alterniflora* and *S. patens*. These findings highlight that optimal camera choice depends on site conditions and dominant vegetation types rather than band quantity alone.

Considering cost and efficiency, the 5-band RedEdge-MX Red camera offered the best balance. The 10-band system was nearly twice as expensive (~ $8,000 vs. ~ $4,500 USD in 2024) and required vastly longer processing—about 22× more time for image stitching (32 h 39 min vs. 1 h 29 min) and 2× longer for classification (16 h 53 min vs. 9 h 30 min). Even the 5-band Blue required unexpectedly long orthomosaic processing (25 h 41 min), possibly due to limited software optimization. Given its efficiency, accuracy, and lower cost, the 5-band Red camera represents a practical, high-performance option for salt marsh vegetation mapping. Although the Dual Camera System delivered marginally higher accuracy (< 1 %), the additional financial and computational costs outweigh these minor gains, demonstrating that greater data volume is not necessarily the best solution for ecological monitoring.

4.2 Research directions

While multispectral drone imagery has advanced salt marsh mapping, opportunities remain to broaden and refine these methods. The present study applied a Random Forest classifier to two salt marsh sites in Aulac, New Brunswick; future work should test this approach across additional regions to evaluate its transferability and robustness. Classification accuracy could be improved through parameter tuning or by applying deep-learning algorithms to capture complex spatial and spectral patterns (Zheng et al., 2022). Soft ("fuzzy") classification methods also warrant exploration, as they can better represent mixed vegetation in heterogeneous marsh environments (Yang et al., 2020). Integrating drone imagery with complementary data sources such as optical or radar satellite and LiDAR data (Slagter et al., 2020; Gray et al., 2018) offers further potential to enhance accuracy. Continued development of multi-source data fusion and dimensionality-reduction techniques will help optimize both precision and efficiency in salt marsh mapping.

5 Conclusions

Our study comparing 5-band and 10-band multispectral drone imagery for salt marsh vegetation mapping shows that cost-efficient configurations, such as the 5-band RedEdge-MX

This contribution has been peer-reviewed. The double-blind peer-review was conducted on the basis of the full paper.
https://doi.org/10.5194/isprs-annals-XI-M-1-2026-39-2026

camera, can achieve classification accuracies comparable to more complex systems. The modest accuracy gains of the 10-band Dual Camera System do not justify its substantially higher cost and processing time where efficiency is a priority. Results emphasize the importance of selecting sensors based on project objectives and site conditions, as the relevance of specific spectral bands—particularly near-infrared and red-edge—varies among environments. Incorporating preliminary analyses of band importance can help tailor monitoring approaches to local vegetation and habitat characteristics, improving classification outcomes. Overall, our findings support more practical and scalable approaches to wetland monitoring, enabling efficient use of resources without compromising data quality. The insights provided here also inform policy and management strategies aimed at protecting salt marsh ecosystems, which play critical roles in biodiversity, coastal resilience, and carbon sequestration.

6 Acknowledgements

We thank Swarna Naojee, Olivia Hanson, Jonathan Linihan, Alexa Stack Mills, and Jenna Watson for assisting in the field. We thank Nic McLellan from Ducks Unlimited Canada and Jeff Ollerhead from Mount Allison University for information and feedback.

7 References

Ahmed, O.S., Shemrock, A., Chabot, D., Dillon, C., Williams, G., Wasson, R., Franklin, S.E., 2017. Hierarchical land cover and vegetation classification using multispectral data acquired from an unmanned aerial vehicle. Int. J. Remote Sens., 38, 2037–2052. doi.org/10.1080/01431161.2017.1294781.

Anne, N.J.P., Abd-Elrahman, A.H., Lewis, D.B., Hewitt, N.A., 2014. Modeling soil parameters using hyperspectral image reflectance in subtropical coastal wetlands. *Int. J. Appl. Earth Obs. Geoinf*., 33, 47–56. doi.org/10.1016/j.jag.2014.04.007.

Artigas, F.J., Yang, J., 2006. Spectral discrimination of marsh vegetation types in the New Jersey Meadowlands, USA. *Wetlands*, 26, 271–277. doi.org/10.1672/0277-5212(2006)26[271:SDOMVT]2.0.CO;2.

Breiman, L., 2001. Random forests. *Mach. Learn.*, 45, 5–32. doi.org/10.1023/A:1010933404324.

Cracknell, A.P., 2018. The development of remote sensing in the last 40 years. *Int. J. Remote Sens.*, 39, 8387–8427. doi.org/10.1080/01431161.2018.1550919.

Desplanque, C., Mossman, D.J., 2004. Tides and their seminal impact on the geology, geography, history, and socio-economics of the Bay of Fundy, Eastern Canada. *Atl. Geol.*, 40. doi.org/10.4138/729.

Doughty, C., Cavanaugh, K., 2019. Mapping coastal wetland biomass from high resolution unmanned aerial vehicle (UAV) imagery. *Remote Sens*., 11, 540. doi.org/10.3390/rs11050540.

Gilbertson, J.K., Van Niekerk, A., 2017. Value of dimensionality reduction for crop differentiation with multi-temporal imagery and machine learning. *Comput. Electron. Agric.*, 142, 50–58. doi.org/10.1016/j.compag.2017.08.024.

Gitelson, A.A., Gritz, Y., Merzlyak, M.N., 2003. Relationships between leaf chlorophyll content and spectral reflectance and algorithms for non-destructive chlorophyll assessment in higher plant leaves. *J. Plant Physiol*., 160, 271–282. doi.org/10.1078/0176-1617-00887.

Gray, P., Ridge, J., Poulin, S., Seymour, A., Schwantes, A., Swenson, J., Johnston, D., 2018. Integrating drone imagery into high resolution satellite remote sensing assessments of estuarine environments. *Remote Sens*., 10, 1257. doi.org/10.3390/rs10081257.

Haralick, R.M., Shanmugam, K., Dinstein, I., 1973. Textural features for image classification. *IEEE Trans. Syst. Man Cybern*., SMC-3, 610–621. doi.org/10.1109/TSMC.1973.4309314.

Huang, Y., Lu, C., Jia, M., Wang, Z., Su, Y., Su, Y., 2023. Plant species classification of coastal wetlands based on UAV images and object-oriented deep learning. *Biodivers*. Sci., 31, 22411. doi.org/10.17520/biods.2022411.

Klemas, V., 2013. Remote sensing of coastal wetland biomass: an overview. *J. Coast. Res*., 29, 1016–1028. doi.org/10.2112/JCOASTRES-D-12-00237.1.

LaRocque, A., Phiri, C., Leblon, B., Pirotti, F., Connor, K., Hanson, A., 2020. Wetland mapping with Landsat 8 OLI, Sentinel-1, ALOS-1 PALSAR, and LiDAR data in Southern New Brunswick, Canada. *Remote Sens*., 12, 2095. doi.org/10.3390/rs12132095.

Li, N., Lu, D., Wu, M., Zhang, Y., Lu, L., 2018. Coastal wetland classification with multiseasonal high-spatial resolution satellite imagery. *Int. J. Remote Sens*., 39, 8963–8983. doi.org/10.1080/01431161.2018.1500731.

Liao, H., Wdowinski, S., Li, S., 2020. Regional-scale hydrological monitoring of wetlands with Sentinel-1 InSAR observations: case study of the South Florida Everglades. *Remote Sens. Environ*., 251, 112051. doi.org/10.1016/j.rse.2020.112051.

McEliece, R., Hinz, S., Guarini, J.M., Coston-Guarini, J., 2020. Evaluation of nearshore and offshore water quality assessment using UAV multispectral imagery. *Remote Sens*., 12, 2258. doi.org/10.3390/rs12142258.

Mutanga, O., Skidmore, A.K., 2004. Narrow band vegetation indices overcome the saturation problem in biomass estimation. *Int. J. Remote Sens*., 25, 3999–4014. doi.org/10.1080/01431160310001654923.

Nardin, W., Taddia, Y., Quitadamo, M., Vona, I., Corbau, C., Franchi, G., Staver, L.W., Pellegrinelli, A., 2021. Seasonality and characterization mapping of restored tidal marsh by NDVI imageries coupling UAVs and multispectral camera. *Remote Sens*., 13, 4207. doi.org/10.3390/rs13214207.

Norris, G.S., LaRocque, A., Leblon, B., Barbeau, M.A., Hanson, A.R., 2024. Comparing pixel- and object-based approaches for classifying multispectral drone imagery of a salt marsh restoration and reference site. *Remote Sens*., 16, 1049. doi.org/10.3390/rs16061049.

Slagter, B., Tsendbazar, N.E., Vollrath, A., Reiche, J., 2020. Mapping wetland characteristics using temporally dense Sentinel-1 and Sentinel-2 data: a case study in the St. Lucia Wetlands, South Africa. *Int. J. Appl. Earth Obs. Geoinf*., 86, 102009. doi.org/10.1016/j.jag.2019.102009.

Sun, C., Li, J., Liu, Y., Liu, Y., Liu, R., 2021. Plant species classification in salt marshes using phenological parameters derived from Sentinel-2 pixel-differential time-series. *Remote Sens. Environ*., 256, 112320. doi.org/10.1016/j.rse.2021.112320.

Turpie, K.R., 2013. Explaining the spectral red-edge features of inundated marsh vegetation. *J. Coast. Res*., 29, 1111–1117. doi.org/10.2112/JCOASTRES-D-12-00209.1.

Wang, C., 2021. At-sensor radiometric correction of a multispectral camera (RedEdge) for sUAS vegetation mapping. *Sensors*, 21, 8224. doi.org/10.3390/s21248224.

Xing, H., Feng, H., Fu, J., Xu, X., Yang, G., 2019. Development and application of hyperspectral remote sensing. In: Computer and Computing Technologies in Agriculture. IFIP Advances in Information and Communication Technology, Vol. 546, 271–282.

Yang, Z., D'Alpaos, A., Marani, M., Silvestri, S., 2020. Assessing the fractional abundance of highly mixed salt marsh vegetation using random forest soft classification. *Remote Sens*., 12, 3224. doi.org/10.3390/rs12193224.

Zhang, C., Gong, Z., Qiu, H., Zhang, Y., Zhou, D., 2021. Mapping typical salt marsh species in the Yellow River Delta Wetland supported by temporal-spatial-spectral multidimensional features. *Sci. Total Environ*., 783, 147061. doi.org/10.1016/j.scitotenv.2021.147061.

Zheng, J.Y., Hao, Y.Y., Wang, Y.C., Zhou, S.Q., Wu, W.B., Yuan, Q., Gao, Y., Guo, H.Q., Cai, X.X., Zhao, B., 2022. Coastal wetland vegetation classification using pixel-based, object-based and deep learning methods based on RGB-UAV. *Land*, 11, 2039. doi.org/10.3390/land11112039.